Australasian Physical & Engineering Sciences in Medicine (2019) 42:1141–1152
https://doi.org/10.1007/s13246-019-00816-8

SCIENTIFIC PAPER

Comprehensive assessment of image quality in synthetic and digital mammography: a quantitative comparison

Patrizio Barca[1,2] · Rocco Lamastra[1,2] · Giacomo Aringhieri[3] · Raffaele Maria Tucciariello[1,2] · Antonio Traino[4] · Maria Evelina Fantacci[1,2]

Received: 29 July 2019 / Accepted: 3 November 2019 / Published online: 14 November 2019

Abstract

Recent advances in digital breast tomosynthesis (DBT) technology were focused on the reconstruction of 2D "Synthesized Mammograms" (SMs) from DBT dataset. The introduction of SMs could avoid an additional digital mammography (DM) which is often required in complement to DBT examinations. Therefore, breast absorbed dose and compression time can be significantly reduced in DBT+SM procedures with respect to DBT+DM modality. However, to date, a limited number of studies have objectively characterised the image quality of SMs with respect to DM images. Therefore, the aim of this phantom study was to comprehensively compare SMs and DM images in terms of several image quality parameters. A Selenia Dimensions system (Hologic, Bedford, Mass, USA) was employed in this work. Five different phantoms were adopted to study noise, contrast and spatial resolution properties of the images. Specifically, noise power spectrum (NPS), maps of signal-to-noise ratio (SNR), contrast-to-noise ratio (CNR), modulation transfer function (MTF) and contrast-detail (CD) thresholds were evaluated both for SM and DM modalities. SMs were characterised by different texture, noise and SNR spatial distribution properties with respect to DM images. Additionally, while in some conditions SM provides higher CNR than DM, lower overall performances in terms spatial resolution and CD curves were found in comparison to DM images. Therefore, given the great benefits of SMs in terms of dose and compression time saving, further clinical investigations on SMs image quality properties could be of practical interest to integrate our findings.

Keywords Synthetic mammography · Digital mammography · Image quality · Digital breast tomosynthesis · Contrast-detail analysis · C-view™

Introduction

Digital breast tomosynthesis (DBT) has been recently introduced in clinical practice to reduce the inherent tissue overlapping associated to Digital Mammography (DM), facilitating discrimination between normal tissue and lesions [1–3]. DBT has been firstly employed in conjunction with DM [4], since the detection of microcalcifications on DBT images resulted often difficult [5, 6]. In addition, the DBT plus DM modality could be useful to better compare new studies with previous DM examinations. Following this approach, some studies have shown that DBT in combination with DM can improve cancer detection rates and reduce false positive findings [6–11]. However, this dual-acquisition modality results in increasing patient dose and breast compression time compared to DM or DBT alone. Therefore, to avoid DM acquisitions additional to DBT procedures, some vendors offer the possibility of reconstructing two dimensional (2D) synthesized mammograms (SMs) from DBT dataset [5, 12–15]. SMs are obtained from DBT through a vendor-specific algorithm that combines DBT data acquired from different angles into a single 2D mammography-like image [5, 12–14, 16, 17]; e.g. SMs can be generated through a maximum intensity projection created from collapsing the DBT image set to a single 2D image [18]. Thus, the aim

✉ Patrizio Barca
patrizio.barca@df.unipi.it

1 Department of Physics, University of Pisa, Largo Bruno Pontecorvo 3, 56127 Pisa, Italy

2 INFN, Pisa Section, Pisa, Italy

3 Department of Translational Research and of New Technologies in Medicine and Surgery, University of Pisa, Pisa, Italy

4 Unit of Medical Physics, Pisa University Hospital "Azienda Ospedaliero-Universitaria Pisana", Pisa, Italy

of SMs is to provide a useful 2D image complementary to DBT slices, highlighting important features that could be less evident in DBT images.

The replacement of DBT plus DM acquisition with DBT plus SM represents an important step toward the ALARA (As Low As Reasonably Achievable) principle, especially in screening programs in which is essential to achieve the lowest dose compatible with the clinical task. Nevertheless, SMs exhibit different image quality properties as compared to DM images, due to the reconstruction algorithm involved in the image generation process [14, 16, 17]. In this regard, a number of studies have investigated the clinical performances of SMs in comparison to DM images and similar results were achieved with both modalities [13, 19–22]. In addition, few studies have objectively compared some aspects of SMs and DM image quality [23–25]. More in detail, in a retrospective study, Alshafeiy and colleagues compared assessments of breast density (BI-RADS categories) on SMs and DM images [13]. They concluded that SMs is comparable with DM images in assessment of breast density, although they found some variability between readers. Another retrospective observer performance study was conducted by Zuley et al. [19]. Comparable performances in terms of probability of malignancy ratings were found in SMs and DM, even in combination with DBT. A recent study performed by Zuckerman et al. aimed to evaluate the implementation of SMs in a population screened with SMs/DBT and they compared recall rates and cancer detection rates to previous outcomes of DM/DBT screening [20]. Similar outcomes were obtained in screening with SMs/DBT and DM/DBT imaging. In agreement with previous studies, Wahab and co-workers found similar frequency for detection of calcifications and BIRADS assessment in SMs and DM images [21]. Additionally, the role of SMs in comparison to DM was discussed by Murphy et al. [22]. Even though no cancers were missed when using SMs alone, they concluded that the full DBT dataset needs to be reviewed to have confidence in diagnosing breast malignancies.

In spite of these encouraging subjective results, only few studies have objectively compared SMs and DM image quality, providing different conclusions [23–25]. In their phantom study Nelson et al. compared CNR, noise and texture properties of SMs and DM images [23]. In comparison to DM, better depiction of objects of specific size and contrast was found in SMs, but these images offered poorer overall resolution and noise properties. Ikejimba and collaborators conducted a contrast-detail phantom study by assessing detectability reader performances in SMs, DBT and DM images [24]. Significantly lower performances were exhibited by SMs in comparison to DM or DBT for all imaging conditions. A more recent phantom study conducted by Baldelli and colleagues analysed sizes and contrasts of several patterns of microcalcifications, shapes and contrasts of circular masses, as well as NPS of background regions [25]. They concluded that SMs did not exhibit significant differences with respect to DM images in terms of image quality. Even though these studies have been carried out by considering appropriate metrics, only a limited number of parameters were analysed.

Given the aforementioned scenario, further investigations on the objective image quality of SMs could be of practical interest. For this reason, the purpose of this study was to comprehensively compare the image quality of SMs with respect to DM images in terms of several parameters. More in detail, noise, texture, contrast and spatial resolution properties of SMs and DM images have been evaluated and a comparison between the two modalities has been carried out.

Methods

Phantoms

Five different phantoms were employed in this study. Specifically, a $30 \times 24 \times 4$ cm^3 homogeneous poly-methylmethacrylate (PMMA) plate was employed to evaluate noise spectral properties and signal-to-noise ratio maps of the images. Two phantoms were adopted to assess contrast-to-noise ratio for low-contrast objects: the Mammographic Accreditation phantom (ACR model 18-220, Fluke Biomedical, Everett, WA, USA), which contains five different size circular low-contrast "masses" to simulate tumors (Fig. 1); the TORMAM phantom (Leeds Test Objects Ltd., North Yorkshire, UK), which includes 6 groups of 3 low-contrast detail subgroups (Fig. 2). A home-made PMMA phantom (Fig. 3) which incorporates a 12.5 µm tungsten wire was expressly assembled to evaluate the spatial resolution of the images. The wire was fixed with an angle of 3° with respect to the longer side of a rectangular PMMA support. The final thickness of the PMMA support was 2 mm. Finally, the CDMAM phantom (v. 3.4, Artinis Medical Systems, Elst, The Netherlands) was employed in contrast-detail analysis (Fig. 4).

Image acquisition

A Selenia Dimensions system (Hologic, Bedford, Mass, USA) was employed to acquire images of the five phantoms in DBT and DM modalities. This device provides three different anode-filter combinations: W-Rh and W-Ag for DM modality, W-Al for DBT modality. The system covers an angular range of 15° in DBT modality, acquiring 15 projections. All the acquisitions were performed by employing the automatic exposure parameters (AE, Auto-Filter mode) set by the device in both modalities. Specifically, for the ACR, TORMAM and the home-made phantom, the exposure

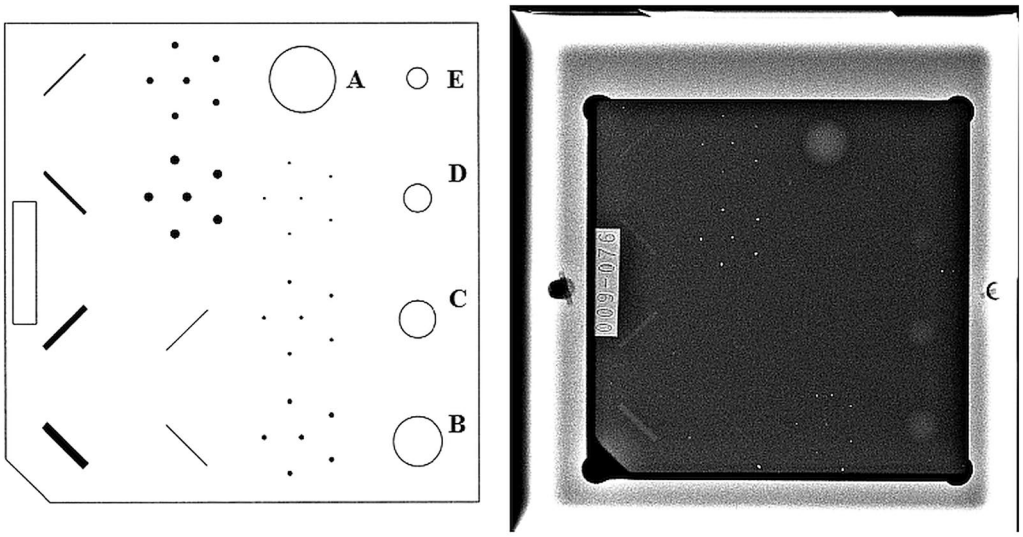

Fig. 1 A schematic representation of the ACR phantom (left panel). Circular inserts A–E were employed for CNR analysis; insert sizes are presented in Table 2. In the right panel, a DM image of the phantom is shown

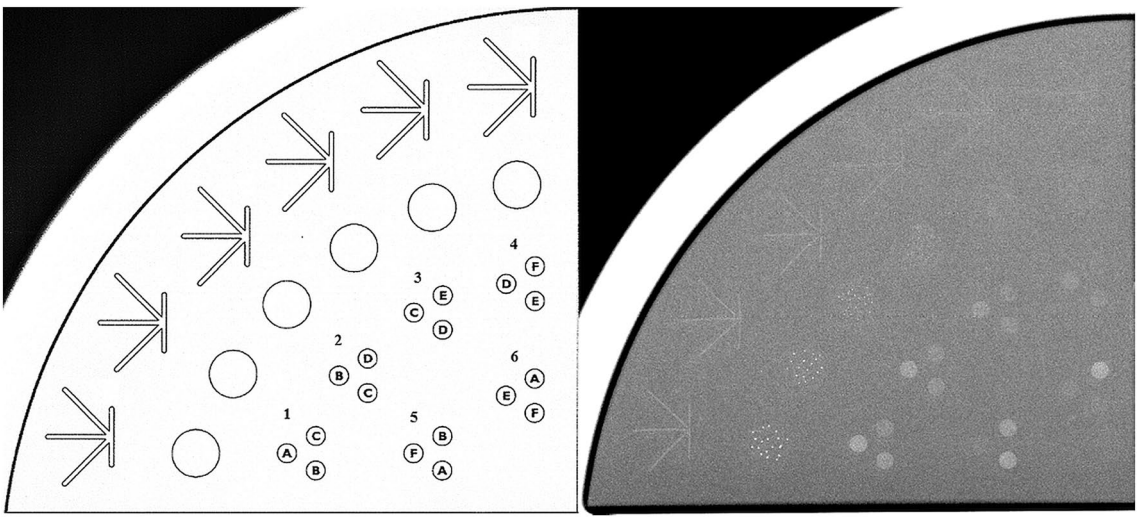

Fig. 2 A schematic representation of the TORMAM phantom (left panel). Clusters of circular inserts 1–6 were employed for CNR analysis (Table 3). Each letter A-F is associated to a specific contrast value. More in detail, inserts A correspond to 4% nominal contrast, B to 3%, C to 2%, D to 1.5%, E to 1% and F to 0.5% [30]. In the right panel, a DM image of the phantom is shown

parameters were derived from the AE settings of 4 cm thick PMMA plate. To match the 4 cm PMMA attenuation equivalence, the TORMAM phantom was placed on top of 2.5 cm of PMMA [26]. The home-made phantom with a 12.5 µm tungsten wire was placed under 4 cm of PMMA, while the composition of ACR phantom approximates the attenuation of 4 cm thick PMMA plate [26–30]. For the CDMAM phantom the acquisition parameters were referred to the AE settings of 5 cm thick PMMA plate, as suggested by quality assurance protocols and international guidelines [27–31]. Table 1 summarises the image acquisition settings for both DBT and DM modalities. SMs (SM version: C-view® 2.0.1.1) were automatically reconstructed by the system from DBT acquisitions.

Image analysis

Noise, texture, contrast and spatial resolution properties were evaluated through the analysis of noise power spectrum (NPS), signal-to-noise ratio (SNR), contrast-to-noise ratio (CNR), modulation transfer function (MTF) and

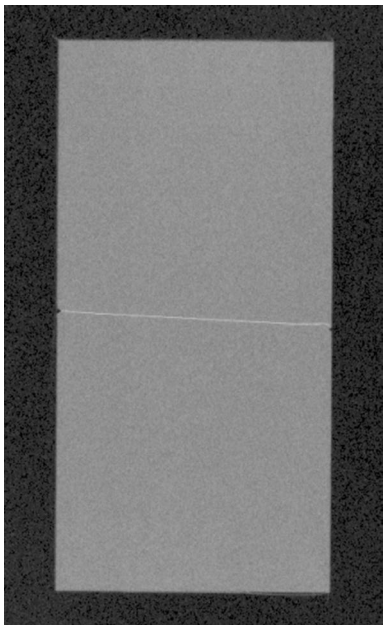

Fig. 3 Image of the home-made phantom. A tungsten wire tilted by 3° was placed between 2 thin PMMA plates (2 mm of total thickness) to measure the oversampled LSF of the system. The diameter of the wire was 12.5 µm

contrast-detail (CD) threshold. In this study were considered processed (for presentation) DM images.

Images and data analysis were performed by means of ImageJ (Wayne Rasband, National Institute of Health, USA), Origin (OriginLab Corporation, MA, USA) and Matlab (The MathWorks, Inc., MA, USA) software packages. The free available CDCOM and CDMAM Analyser v. 1.5.5 software were employed for CD evaluation (www.euref.org) [32].

NPS

The 2D-NPS was computed through the following relationship [33]:

$$NPS(f_x,f_y) = \frac{\Delta x \cdot \Delta y}{N_x \cdot N_y} \cdot < \left| FFT\left(ROI_n(x,y)\right)\right|^2 > \quad (1)$$

where Δx and Δy are the pixel sizes, N_x and N_y the number of pixels in each direction within the region of interest (ROI) and $ROI_n(x,y)$ is a "noise" ROI. The "noise" image was obtained by subtracting two images acquired under the same conditions. Consequently, a factor 1/2 was applied to Eq. (1). The Fast Fourier Transform (FFT) was applied to 50 $ROIs_n$ of 128×128 pixels and the ensemble average was considered to obtain the final 2D-NPS. The ImageJ software package was employed for image analysis. To better emphasise the NPS properties, the 2D-NPS was averaged along the

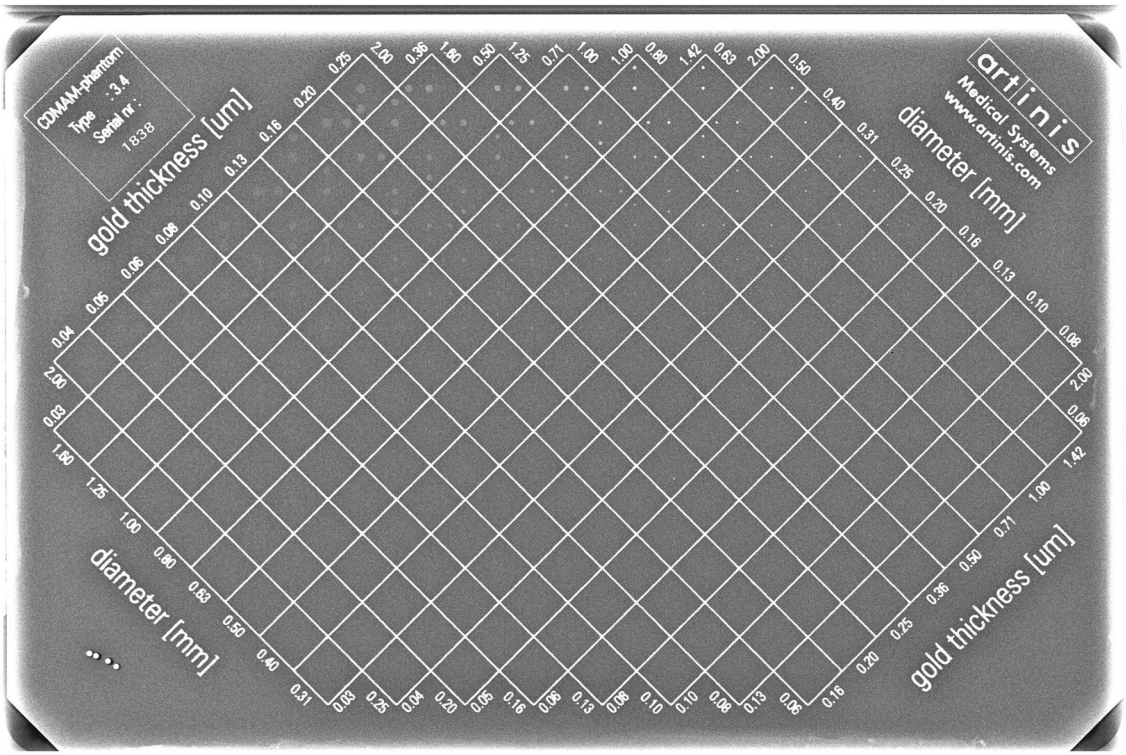

Fig. 4 Image of the CDMAM 3.4 phantom. This phantom was employed for contrast-detail analysis, as suggested by international guidelines [27–30]

Table 1 System settings for DBT and DM acquisition modalities

Phantoms	*ACR*, *TORMAM*, *PMMA*, *PMMA+W wire*		*CDMAM*	
Modality	DBT	DM	DBT	DM
Anode/filter	W/Al	W/Rh	W/Al	W/Rh
Grid	Out	In	Out	In
Tube voltage (kVp)	30	28	33	31
Tube load (mAs)	35	75	35	80

f_x (horizontal), f_y (vertical) and radial directions for both SM and DM modalities. To directly appreciate the NPS results in terms of texture appearance, a visual inspection of the phantom images was also performed.

SNR maps

In order to carry out a complete study of the noise properties, 30 images of the homogeneous PMMA phantom were acquired with identical settings. For each pixel, the average and the standard deviation (SD) across the 30 images were computed in order to determine average and SD maps. Then, a pixel-by-pixel SNR map was obtained from the ratio between the average map and SD map. The ImageJ software package was employed for generating SNR maps. The following non-uniformity index (NUI) was adopted to make a quantitative comparison between SMs and DM SNR maps:

$$NUI = \frac{\max\left(\overline{PV}_{ROI_i}\right) - \min\left(\overline{PV}_{ROI_i}\right)}{\left[\frac{\max\left(\overline{PV}_{ROI_i}\right)+\min\left(\overline{PV}_{ROI_i}\right)}{2}\right]} \quad (2)$$

where $\overline{PV}_{ROI_i}$ is the mean pixel value within the i_{th}-ROI. To compute the NUI using Eq. (2) a large ROI was selected in the SNR map for both SM and DM modalities. This ROI was obtained by excluding about 1 cm from the edges of the original image, in order to avoid edge effects. A set of sub-ROIs of 100×100 pixels was then adopted and the maximum and minimum $\overline{PV}_{ROI_i}$ were extracted. Furthermore, another sub-region (14×14 cm) of the original images was considered. Specifically, the region was centered at 8 cm from the chest wall side of the images (i.e. the region of the image which usually contains the main part of the breast) and the NUI was computed as described above.

CNR

The CNR was computed in the low contrast inserts of the ACR and TORMAM phantoms (Figs. 1 and 2) using the following relationship [34]:

$$CNR = \frac{\overline{PV}_{insert} - \overline{PV}_{background}}{\sigma_{background}} \quad (3)$$

where PV_{insert} and $\overline{PV}_{background}$ are the mean pixel values in a ROI placed within the insert and in the background region respectively; $\sigma_{background}$ is the standard deviation computed in the ROI placed in the background region. Circular ROIs of a diameter of about 2 mm (i.e. 18 and 30 pixels for SMs and DM images respectively) were employed in both phantoms. The coefficient of variation obtained from 30 images was used to compute the uncertainties in CNR calculation.

MTF

The spatial resolution of SMs and DM images was evaluated by computing the MTF through the Line Spread Function (LSF) method [29, 35]. The home-made phantom with a 12.5 µm tungsten wire (Fig. 3) was placed under 4 cm of PMMA to match the same conditions of the previous mentioned acquisitions (Table 1). The ImageJ software package was used to extract a series of horizontal/vertical profiles which were combined to obtain the over-sampled LSF. The Origin software package was employed to fit the over-sampled LSF using a Gaussian function (G) with an offset: $y(\xi) = y_0 + G(\xi)$; the offset y_0 was subtracted before applying the Fourier Transform (FT); the module of the FT was then computed to obtain the MTF which was finally normalised to the MTF(0) value. The MTF was calculated along the tube travel direction ($\xi = x$, MTF_x) and along the orthogonal direction ($\xi = y$, MTF_y) for both SMs and DM images.

CD analysis

The CDMAM phantom were acquired to assess the contrast-detail curve for each modality. The phantom was placed with a 2 cm thickness of PMMA above and 2 cm thickness below [27–31]. Sixteen different acquisitions of the phantom were performed by slightly moving the phantom each time [27–31, 36] and for each position both SMs and DM images were acquired. The analysis of the images was carried out by using the Matlab environment in order to run the CDMAM Analyser v.1.5.5 software which combines the data from multiple images to obtain the threshold contrast, providing a contrast-detail curve [37, 38].

Results

NPS

The NPS obtained from SMs and DM images is shown in Fig. 5. Specifically, in order to comprehensively investigate spectral noise properties, the radial-, vertical- and horizontal-NPS are presented. Significant differences in radial-NPS shape can be highlighted: in SMs, an evident peak around the spatial frequency of 1 mm^{-1} is expressed; conversely, in DM images, the NPS appears substantially flat along the entire spatial frequency range. Additionally, the NPS shape associated to DM images is quite similar along vertical and horizontal directions, manifesting symmetry properties. On the other hand, although a peak is clearly shown in the vertical-NPS, it is barely visible in the horizontal direction. No symmetry is exhibited in this case. These results are reflected in the texture appearance of the images: the texture of SMs appeared more coarse grained than the texture of DM images, as shown in Fig. 6. This feature can be appreciated on both ACR and TORMAM phantoms.

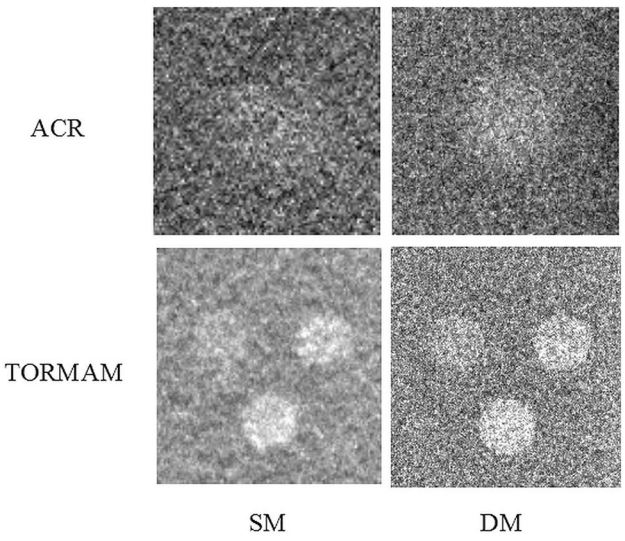

Fig. 6 Comparison of texture granularity between SMs and DM images for ACR and TORMAM low contrast details. Notice a more coarse grained texture associated to SMs with respect to DM images in agreement with the NPS behaviour of Fig. 5

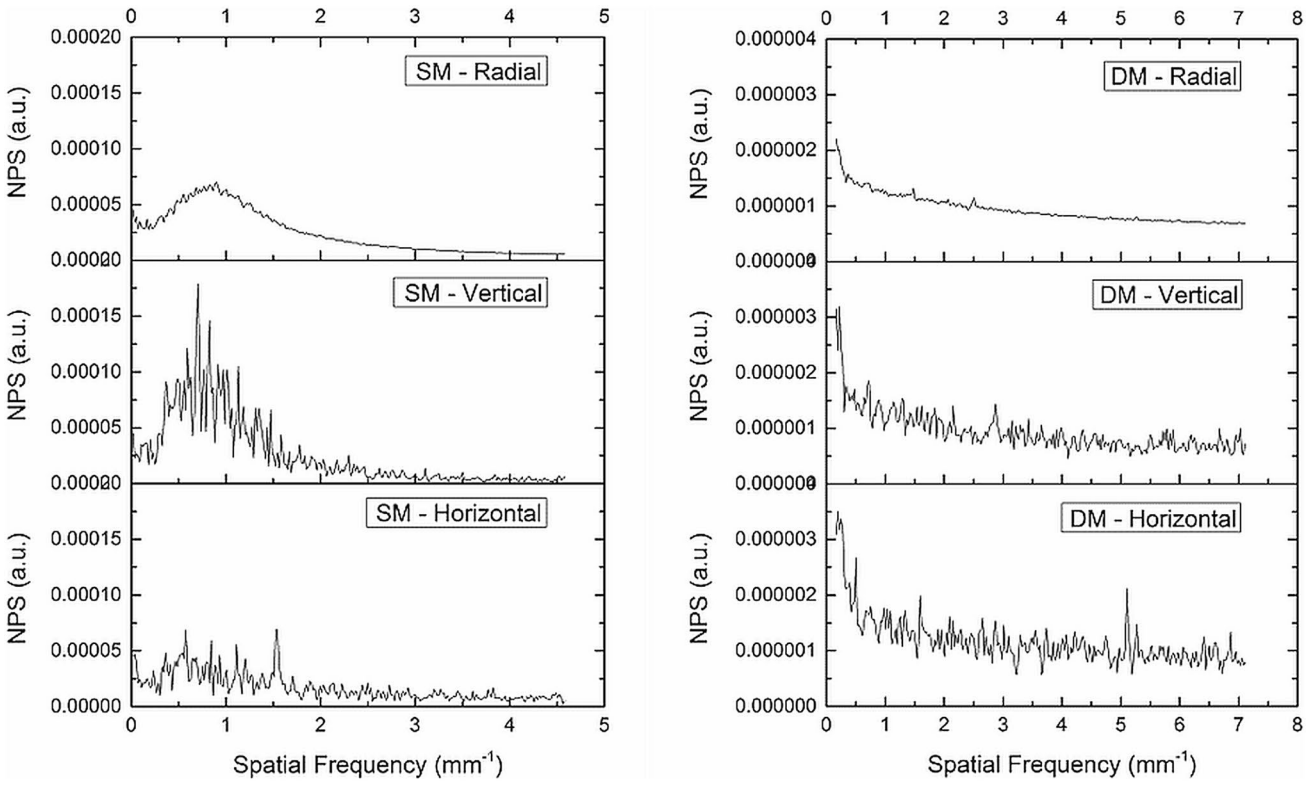

Fig. 5 Comparison between radial, vertical (f_y) and horizontal (f_x) NPS for SM and DM modalities. Notice the presence/absence of a peak in NPS associated to SMs/DM images respectively

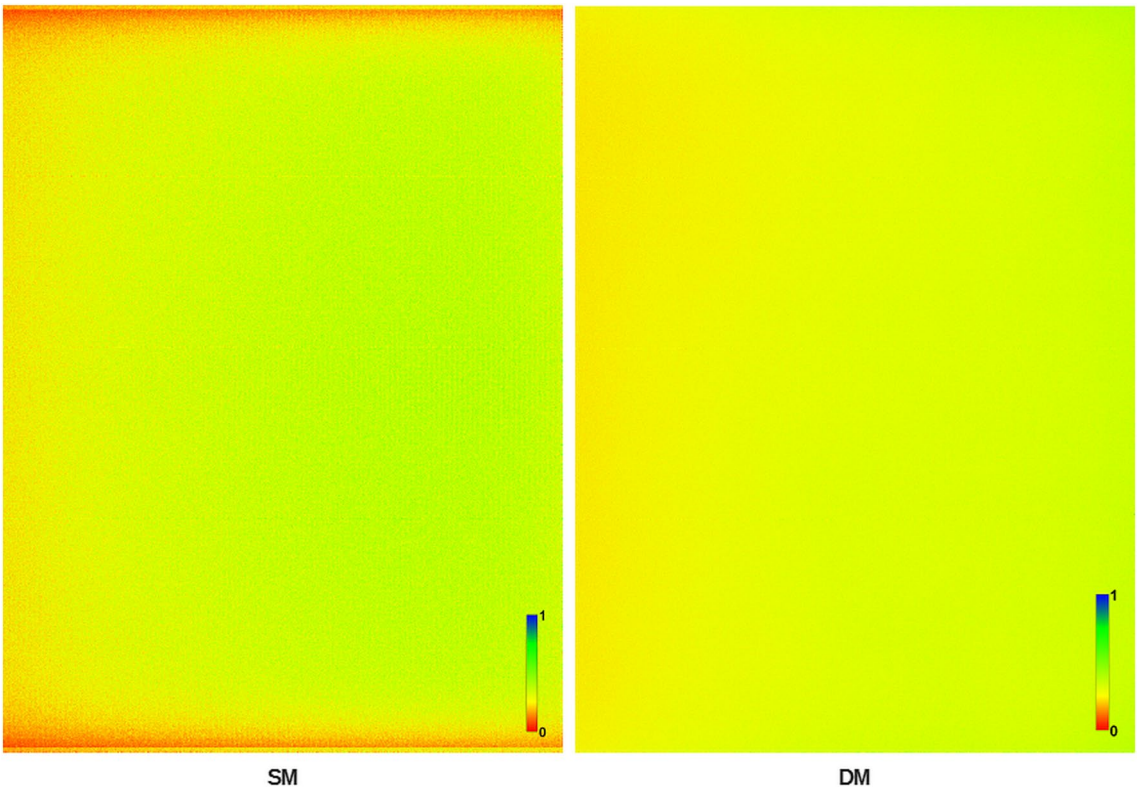

Fig. 7 SNR maps obtained from 30 images of the homogeneous PMMA phantom acquired in the same conditions for SM and DM modalities. The maps were normalised to allow a better visualisation of the SNR distribution across the image

SNR maps

In Fig. 7 normalised SNR maps related to SMs and DM images are presented. Based on a first qualitative comparison, the DM SNR map appears to be more uniform compared to the SM map. Furthermore, in order to conduct a quantitative comparison, the NUI was calculated. Values of 0.61 and 0.26 were obtained for SMs and DM images respectively, confirming the qualitative perception. In addition, SNR maps seem to be similar in terms of SNR spatial distribution within the sub-region close to the chest wall side. The NUI values in this sub-region were 0.15 for SMs and 0.23 for DM images.

CNR

Tables 2 and 3 present the CNR values obtained for low contrast inserts of the ACR and TORMAM phantoms respectively. Before applying the CNR calculation a visual inspection of the images was performed. On this basis, nominal inserts which were not detectable in the images were exluded from the CNR analysis both in SMs and in DMs, as specified in Tables 2 and 3. For the two larger inserts of the ACR phantom, the CNR values obtained in DM images were higher than those obtained in SMs. Conversely, for the two smallest inserts CNR values in SMs were slightly higher than in DM images. Instead, for the TORMAM phantom, CNR values obtained in SMs were higher than those obtained in DM images.

Table 2 CNR values computed from the "masses" included in the ACR phantom (Fig. 1) for both SM and DM modalities

Insert	Diameter (mm)	CNR–SM	CNR–DM
A	2.00	1.40 ± 0.24	2.36 ± 0.07
B	1.00	1.23 ± 0.24	1.42 ± 0.05
C	0.75	0.98 ± 0.22	0.82 ± 0.04
D	0.50	0.67 ± 0.21	0.39 ± 0.04
E	0.25	Not visible	Not visible

MTF

MTFs computed through the LSF approach are shown in Fig. 8 for both SMs and DM images. In detail, MTF associated to DM resulted higher than the MTF of SMs over the entire spatial frequency range, in both x and y directions. No significant differences were found in MTF_x and MTF_y of DM images, while MTF_x was significantly lower than MTF_y.

Table 3 CNR values computed from the low contrast details contained in the TORMAM phantom (Fig. 2) for both SM and DM modalities

Insert group	Insert type	CNR–SM	CNR–DM
	B	2.63 ± 0.30	1.12 ± 0.03
1	A	2.76 ± 0.31	1.69 ± 0.05
	C	1.27 ± 0.21	0.66 ± 0.03
	C	1.12 ± 0.20	0.68 ± 0.03
2	B	1.96 ± 0.25	1.29 ± 0.04
	D	0.93 ± 0.19	0.69 ± 0.03
	D	0.97 ± 0.19	0.55 ± 0.03
3	C	1.34 ± 0.21	0.90 ± 0.03
	E	Not visible	0.48 ± 0.02
	E	Not visible	0.65 ± 0.03
4	D	0.61 ± 0.18	0.70 ± 0.03
	F	Not visible	Not visible
	A	3.34 ± 0.36	1.67 ± 0.05
5	F	Not visible	Not visible
	B	2.21 ± 0.27	1.22 ± 0.04
	F	Not visible	Not visible
6	E	Not visible	0.45 ± 0.02
	A	2.67 ± 0.30	1.91 ± 0.05

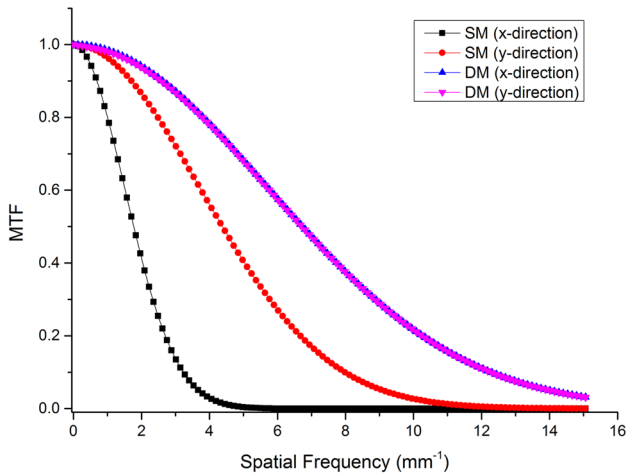

Fig. 8 MTFs computed from SMs and DM images along x- and y-direction. No differences were found between the MTF_x and MTF_y of DM modality. Conversely, MTF_x was lower than MTF_y in SMs within the entire spatial frequency range. Additionally, MTFs of SMs were always lower than MTFs of DM images

for SMs. Table 4 reports the spatial frequencies related to 50%, 20% and 10% MTFs fall off.

CD analysis

Figures 9 and 10 show the results of the CDMAM analysis. Specifically, the probability of correct detection as a function of the disc thickness is presented in Fig. 9 for different disc sizes (diameter of the discs). A threshold at 62.5% correct responses was set for computing contrast detail curves as shown in Fig. 10. The CD curve trend for SMs and DM images was similar; however, the contrast thresholds associated to DM images were lower than the thresholds exhibited by SMs for each considered disc size. For example, for a disc diameter of 0.50 mm, the contrast threshold for DM images was 0.13 µm of gold thickness. For the same diameter, the associated contrast threshold in SMs was 0.30 µm of gold thickness.

Table 4 Spatial frequencies associated to the Nyquist frequency, $MTF_{50\%}$, $MTF_{20\%}$ and $MTF_{10\%}$ along two orthogonal directions

	SM		DM	
	f_x (mm^{-1})	f_y (mm^{-1})	f_y (mm^{-1})	f_y (mm^{-1})
Nyquist frequency	4.6	4.6	7.1	7.1
MTF50%	2.1	4.3	6.7	6.7
MTF20%	2.6	6.7	10.1	10.1
MTF10%	3.1	8.2	12.3	12.3

These values were extracted from MTF curves of Fig. 8

Discussion

Synthesized mammography has been recently introduced to avoid the employment of additional DM to DBT procedures. Previous studies highlighted the benefits of a combined DBT+SM modality in terms of radiation dose and compression time reduction as compared to DBT+DM approach [12, 15–17, 20]. For this reason, a number of clinical studies compared the performances of SMs and DM images associated to specific tasks [13, 19–22]. Additionally, few studies have objectively compared SMs and DM image quality, providing different conclusions [23–25]. Although these studies analysed in great detail some properties of SMs with respect to DM images, only a limited number of image quality parameters was considered.

Therefore, the aim of this study was to conduct a comprehensive comparison between SMs and DM images, by evaluating noise, texture, contrast and spatial resolution properties. Specifically, noise properties of SMs and DM images were investigated through the calculation of the NPS. As shown in Fig. 5, NPS associated to SMs exhibits different shape as compared to DM images. In fact, while DM images are characterised by an almost flat NPS trend within the considered spatial frequency range, a clear peak is shown in NPS of SMs. More in detail, the NPS peak of SMs is centred around 1 mm^{-1} (i.e. in the lower part of the spatial frequency range). In fact, the reconstruction process in SMs introduces noise correlation in the final images

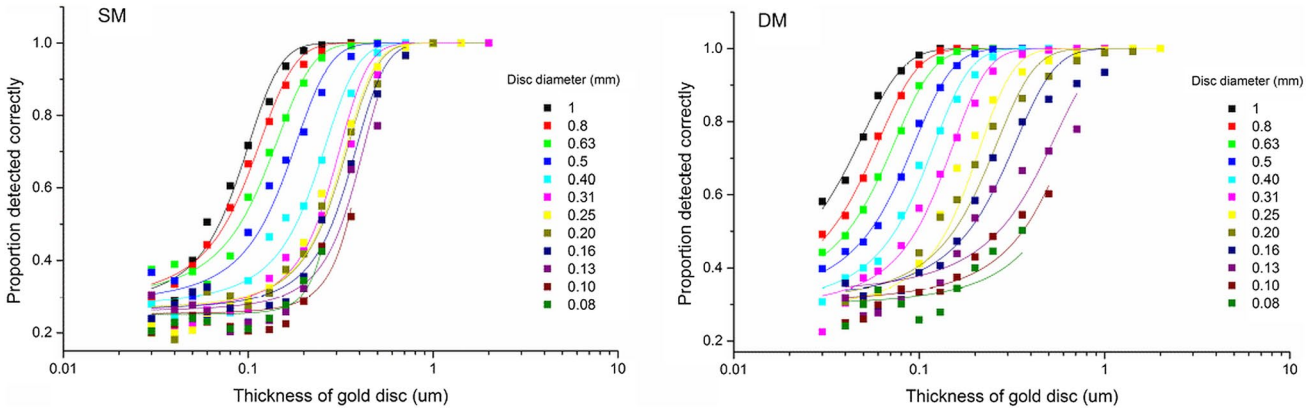

Fig. 9 Results of the CDMAM automated analysis in terms of the proportion of correct detection as a function of the gold disc thickness for SMs and DM images. Data were fitted with a psychometric curve as suggested by international guidelines and previous works [27, 37, 38]. A threshold of 62.5% was adopted to extract values for computing the final CD curves

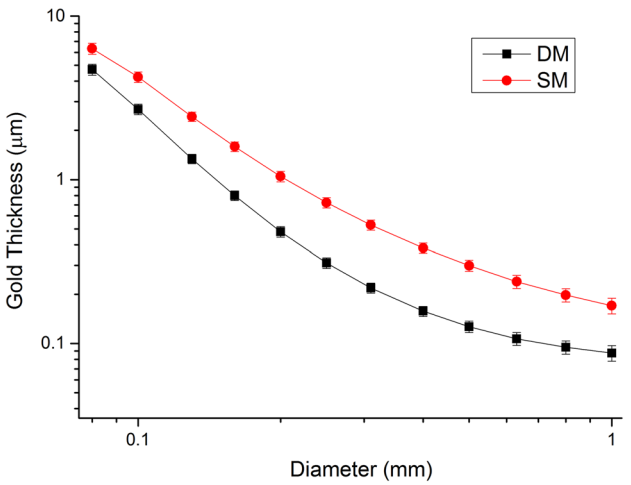

Fig. 10 Predicted CD curves obtained from the CDMAM analysis for SM and DM modalities. Notice the better performances of DM for all considered object sizes. The predicted human thresholds values were obtained by the CDMAM Analyser v.1.5.5 scaling up the automated thresholds using specific factors for each detail diameter [37]

which is expressed by a more coarse grained texture than DM images (Fig. 6). Similar differences in noise texture were found in previous studies [23, 39]. Notice that SMs are reconstructed from tomosynthesis data derived from planar projections at different angles. Each projection is employed in generating tomosynthesis data and therefore noise in each projection influences noise of all image planes, this is also reflected into SMs. Therefore, noise correlation should be expected in these images. In addition, different NPS shapes were obtained along the vertical and horizontal direction in SMs images (Fig. 5). This is probably related to the movement of X ray tube along one direction during the acquisition process and the subsequent reconstruction of the final image. Conversely, no differences were found between vertical and horizontal DM NPS, which exhibits symmetry properties as expected. To further investigate the noise properties of SMs, SNR maps were derived from 30 repeated acquisitions of the homogeneous PMMA phantom and compared to those obtained in conventional DM. These maps were used to compare spatial distribution of SNR between SMs and DM images. From a visual inspection, the SNR map of SMs appears less uniform than the SNR map of DM images. This difference is quantified by the NUI value which results 0.61 for SM and 0.26 for DM modality. Notice that the differences between SNR maps in SMs and DM are less evident in the central region toward the chest wall side of the images, which is the region of the image which usually contains the main part of the breast. In this region, SMs expressed even better results in terms of SNR uniformity (NUI = 0.15 for SMs, NUI = 0.23 for DM images). Notice that the effect of the not-homogeneous irradiation due to the tube motion in tomosynthesis acquisition could be more pronounced in peripheral regions than the central one in which the sub-region was placed. This could partially explain the reason why the NUI of SMs results lower in the sub-region. Besides, changes in SNR within the images (e.g. between central and peripheral regions) could be important when images containing low-contrast features are analysed. In addition, it could be useful to adopt the same approach in further studies by employing heterogeneous phantoms, which could permit a more relevant comparison.

In order to assess CNR in SMs and DM images two phantoms (ACR and TORMAM) were used in this study. These phantoms are specifically designed and widely employed for image quality evaluation [27–31, 40, 41]. Different trends were found in the CNR analysis of the two phantoms. In fact, in ACR images (Table 2) the CNR values determined in DM modality were greater than those computed in SMs for the two larger inserts (type "A" and "B"), but a reverse

situation was found for the two smaller inserts (type "C" and "D"). On the other hand, in TORMAM images (Table 3) the CNR values obtained in SMs were higher than those found in DM images. Similar behaviours were highlighted in a previous study [25]. In this regard, it should be noted that the Hologic SMs reconstruction algorithm attempts to create an image in which some features of interest appear with greater conspicuity than they would in the conventional DM [14]. Slices and regions containing calcification-like and lesion-like characteristics are identified and extra weight is given to these "special" regions when tomosynthesis slices are combined into the final SM image [14]. This could be the reason why most of the CNR values found in SMs were higher than those obtained in DM images. Notice that, even though in TORMAM images the CNR values were higher in SM modality as compared to DM, a lower number of low-contrast inserts were clearly identifiable (Table 3). Furthermore, some appreciable variability is expressed among insert of same nominal contrast and different group (i.e. different location) in the TORMAM phantom for both modalities (e.g. among the "A" inserts in groups 1, 5 and 6, Table 3). Moreover, notice that the uncertainties associated to CNR values in SMs are always significantly greater than those expressed in DM images, implying higher variability in the former case. These results suggest that the employment of CNR as a stand-alone image quality indicator is not properly suitable for comparing two different mammographic modalities, even in clinical studies. Additionally, the obtained results cannot be generalised to all mammographic devices (e.g. different algorithms can be involved in the SMs reconstruction process) as suggested by a previous study [25].

The spatial resolution of the system was evaluated by computing the MTF. Our results show a clear better performance of DM with respect to SM in terms of spatial resolution of the images (Fig. 8; Table 4). No significant differences were found between the x- and y-MTF of DM images. Conversely, in SMs, the y-MTF was significantly higher than x-MTF. This result is probably related to the tube motion along the x-direction during the DBT acquisition process. Our findings were also highlighted in a previous initial analysis [39]. Further investigations could be useful to evaluate how much these results can affect the clinical performances of SMs under different conditions.

Sixteen images of the CDMAM phantom were considered to assess the CD curves in SM and DM modalities, as suggested by international guidelines [27, 28]. Better performances in terms of CD curves were expressed in DM images for all disc diameters as shown in Fig. 10 (i.e. the predicted threshold contrast associated to SM was higher than that obtained in DM for every object size). This result can be partially related to the loss in spatial resolution expressed in MTF analysis (Fig. 8). In addition, ours results confirm those found by Ikejimba and colleagues in a previous study [24].

Based on our results, the SMs offer overall lower performances in terms of almost all considered image quality parameters than DM images. Only CNR analysis on TORMAM phantom shows higher performances of the SMs in comparison to DM images. Even though this study highlights some limits of SMs in terms of objective image quality, previous studies showed acceptable performances of SMs in clinical practice [13, 19–22]. Therefore, in order to have a complete overview of the potential of SM, subjective image quality tests both on standard phantoms and clinical images should integrate our quantitative analysis.

We would like to remark that SMs are only to be used in conjunction with tomosynthesis and not as "stand-alone" modality as DM. Therefore, a complete characterisation of the imaging system in terms of image quality would require the inclusion of tomosynthesis in the analysis. However, a full characterisation of image quality of SMs in comparison to DMs could help to clarify power and limits of this modality.

Some limitations of our study must be recognised. Firstly, the employment of the Fourier metrics in NPS and MTF calculation requires assumptions of linearity and stationarity of the imaging system. These requirements are not strictly achieved in processed ("for presentation") DM images. Additionally, the SMs reconstruction process is based on maximum intensity projection [18], i.e. a non-linear algorithm is involved in images generation. However, the aim of this study was to compare SMs and DMs in their final form i.e. by considering images that would have been analysed by a radiologist. The assumption of small signal linearity and wide-sense stationarity has been tacitly made in our analysis. Nevertheless, even though these results can not simply be generalisable to all possible conditions (e.g. image noise and objects contrast), it is likely that better MTF and NPS results correspond to better spatial resolution and noise properties of a given modality with respect to the other. In addition, the adoption of standard phantoms (i.e. standard conditions under specific exposure settings) should facilitate the comparison of our results with other future studies. Furthermore, even though we employed a home-made phantom for spatial resolution assessment, the high-contrast condition produced by the tungsten wire should be simply reproducible for MTF evaluation.

It should also be noted that our results are strictly valid for the employed system (i.e. only for the Selenia Dimensions device under the above described conditions) and cannot be simply generalised to other mammographic devices. In fact, different performance of the devices hardware, different processing and/or reconstruction methods can be involved in the image generation process and can induce differences in the final image quality. In this regard, more insights on these aspects could be interesting and the presented analysis

could be extended to study the performance of other mammographic devices.

Conclusions

In this study we performed a comprehensive comparison between SM and DM image quality. NPS, SNR, CNR, MTF and CD curves were evaluated in order to investigate noise, contrast and spatial resolution properties of the images. Our results showed overall lower performances and different image quality properties of SMs as compared to DM images. Only in CNR properties SM performed better than DM. Even though further studies are needed to integrate these analysis, this study represents a solid objective evaluation of image quality and these results could be employed as starting point to a more complete investigation on SMs properties.

Acknowledgements This work has been partially supported by the RADIOMA Project, funded by Fondazione Pisa, Technological and Scientific Research Sector, Via Pietro Toselli 29, Pisa. We would like to thank the Unit of Medical Physics "SOC Fisica Sanitaria Firenze ed Empoli—Azienda USL Toscana Centro" for their support.

Compliance with ethical standards

Conflict of interest The authors declare that they have no conflict of interest.

Ethical approval Given that our study is a phantom study, the ethical approval statement is not needed/applicable.

References

1. Sechopoulos I (2013) A review of breast tomosynthesis. Part I. The image acquisition process. Med Phys 40(1):014301
2. Sechopoulos I (2013) A review of breast tomosynthesis. Part II. Image reconstruction, processing and analysis, and advanced applications. Med Phys 40(1):014302
3. Vedantham S, Karellas A, Vijayaraghavan GR, Kopans DB (2015) Digital breast tomosynthesis: state of the art. Radiology 277(3):663–684
4. US Food and Drug Administration (2019) Department of Health and Human Services. Digital Accreditation. https://www.fda.gov/Radiation-EmittingProducts/MammographyQualityStandardsActandProgram/FacilityCertificationandInspection/ucm114148.htm. Accessed 11 June 2019
5. Choi JS, Han BK, Ko EY, Ko ES, Hahn SY, Shin JH, Kim MJ (2016) Comparison between two-dimensional synthetic mammography reconstructed from digital breast tomosynthesis and full-field digital mammography for the detection of T1 breast cancer. Eur Radiol 26(8):2538–2546
6. Skaane P, Bandos AI, Gullien R, Eben EB, Ekseth U et al (2013) Comparison of digital mammography alone and digital mammography plus tomosynthesis in a population-based screening program. Radiology 267(1):47–56
7. Bernardi D, Ciatto S, Pellegrini M et al (2012) Prospective study of breast tomosynthesis as a triage to assessment in screening. Breast Cancer Res Treat 133(1):267–271
8. Ciatto S, Houssami N, Bernardi D et al (2013) Integration of 3D digital mammography with tomosynthesis for population breast-cancer screening (STORM): a prospective comparison study. Lancet Oncol 14(7):583–589
9. Gennaro G, Toledano A, di Maggio C et al (2010) Digital breast tomosynthesis versus digital mammography: a clinical performance study. Eur Radiol 20(7):1545–1553
10. Gur D, Bandos AI, Rockette HE et al (2011) Localized detection and classification of abnormalities on FFDM and tomosynthesis examinations rated under an FROC paradigm. AJR Am J Roentgenol 196(3):737–741
11. Rafferty EA, Park JM, Philpotts LE et al (2013) Assessing radiologist performance using combined digital mammography and breast tomosynthesis compared with digital mammography alone: results of a multicenter, multireader trial. Radiology 266(1):104–113
12. Zuckerman SP, Maidment ADA, Weinstein SP, McDonald ES, Conant EF (2017) Imaging with synthesized 2D mammography differences, advantages, and pitfalls compared with digital mammography. AJR Am J Roentgenol 209(1):222–229
13. Alshafeiy TI, Wadih A, Nicholson BT, Rochman CM, Peppard HR, Patrie JT, Harvey JA (2017) Comparison between digital and synthetic 2D mammograms in breast density interpretation. AJR Am J Roentgenol 209(1):W36–W41
14. Smith AH. Synthesized 2D mammographic imaging theory and clinical performance. C-view white paper. https://www.lowdose3d.com/images/C-View-White-Paper.pdf. Accessed 9 June 2019
15. Svahn TM, Houssami N, Sechopouous I, Mattson S (2015) Review of radiation dose estimates in digital breast tomosynthesis relative to those in two-view full-field digital mammography. Breast 24(2):93–99
16. Durand MA (2018) Synthesized mammography: clinical evidence, appearance, and implementation. Diagnostics 8(2):E22
17. Ratanaprasatporn L, Chikarmane SA, Giess CS (2017) Strengths and weaknesses of synthetic mammography in screening. RadioGraphics 37(7):1913–1927
18. U.S. Food Drug Administration (2012) P080003/S001 hologic selenia dimensions 3D system, FDA executive summary. FDA, College Park
19. Zuley ML, Guo B, Catullo VJ, Chough DM, Kelly AE, Lu AH et al (2014) Comparison of two-dimensional synthesized mammograms versus original digital mammograms alone and in combination with tomosynthesis images. Radiology 271(3):664–671
20. Zuckerman SP, Conant EF, Keller BM et al (2016) Implementation of synthesized two-dimensional mammography in a population-based digital breast tomosynthesis screening program. Radiology 281(3):730–736
21. Wahab RA, Lee SJ, Zhang B, Sobel L, Mahoney MC (2018) A comparison of full-field digital mammograms versus 2D synthesized mammograms for detection of microcalcifications on screening. Eur J Radiol 107:14–19
22. Murphy MC, Coffey L, O'Neill AC, Quinn C, Prichard R, McNally S (2018) Can the synthetic C view images be used in isolation for diagnosing breast malignancy without reviewing the entire digital breast tomosynthesis data set? Ir J Med Sci 187(4):1077–1081
23. Nelson JS, Wells JR, Baker JA, Samei E (2016) How does c-view image quality compare with conventional 2D FFDM? Med Phys 43(5):2538
24. Ikejimba LC, Glick SJ, Samei E, Lo JY (2016) Assessing task performance in FFDM, DBT, and synthetic mammography using uniform and anthropomorphic physical phantoms. Med Phys 43(10):5593

25. Baldelli P, Bertolini M, Contillo A, Della Gala G, Golinelli P, Pagan L, Rivetti S, Taibi A (2018) A comparative study of physical image quality in digital and synthetic mammography from commercially available mammography systems. Phys Med Biol 63(16):165020
26. Fluke Biomedical (2005) Mammographic accreditation phantom operators manual, Manual No. 18-220-1 Rev. 2
27. European Reference Organisation for Quality Assured Breast Screening and Diagnostic Services (2006) European guidelines for quality assurance in breast cancer screening and diagnosis. (EUREF)
28. European Reference Organisation for Quality Assured Breast Screening and Diagnostic Services (2013) European guidelines for quality assurance in breast cancer screening and diagnosis—Supplement EUREF
29. European Reference Organisation for Quality Assured Breast Screening and Diagnostic Services (2018) Protocol for the quality control of the physical and technical aspects of digital breast tomosynthesis systems. (EUREF)
30. European Federation of Organisations For Medical Physics. Quality controls in digital mammography (2015) Protocol of the EFOMP mammo working group
31. The National Cancer Screening Service Board (2008) Guidelines for quality assurance in mammography screening. The National Cancer Screening Service Board, Dublin
32. https://medphys.royalsurrey.nhs.uk/nccpm/. Accessed 27 June 2019
33. Siewerdsen JH, Cunningham IA, Jaffray DA (2002) A framework for noise-power spectrum analysis of multidimensional images. Med Phys 29(11):2655–2671
34. Goodsitt MM, Chan HP, Schmitz A, Zelakiewicz S, Telang S, Hadjiiski L et al (2014) Digital breast tomosynthesis: studies of the effects of acquisition geometry on contrast-to-noise ratio and observer preference of low-contrast objects in breast phantom images. Phys Med Biol 59(19):5883–5902
35. Bushberg JT, Seibert JA, Leidholdt EM Jr, Boone JM (2012) The essential physics of medical imaging, 3rdrf edn. Lippincott Williams & Wilkins, Philadelphia
36. Artinis Medical Systems (2010) Contrast-detail phantom CDMAM 3.4 Manual - Version 7
37. Young KC, Brookes E, Hudson W, Halling-Brown MD (2012) CDMAM Analyser: Software and instruction manual for automated determination of threshold contrast—Version 1.5.5
38. Karssemeijer N, Thijssen MAO (1996) Determination of contrast-detail curves of mammography systems by automated image analysis. Digital Mammography. Elsevier, Amsterdam, pp 155–160
39. Barca P, Lamastra R, Caramella D, Traino AC, Tucciariello RM, Fantacci ME (2019) Image quality comparison between digital and synthetic mammograms—a qualitative and quantitative phantom study. Proceedings of the 11th International Joint Conference on Biomedical Engineering Systems and Technologies (BIOSTEC 2019), Vol 2: BIOIMAGING, pp. 129–136
40. The Royal Australian and New Zealand College of Radiologists (2018) Guidelines for Quality Control Testing for Digital (CR & DR) Mammography—Version 4.0
41. The American College of Radiology (1999) Mammography. Quality control manual. The American College of Radiology, Reston